DYNAMICS OF BUBBLE OSCILLATION IN CONSTRAINED MEDIA AND MECHANISMS OF VESSEL RUPTURE IN SHOCK WAVE LITHOTRIPSY

Pei Zhong, Yufeng Zhou, and Songlin Zhu
Duke University, Durham, NC 27708, USA

Abstract

Rupture of small blood vessels is a primary feature of the tissue injury associated with shock wave lithotripsy (SWL), and cavitation has been implicated as a potential mechanism. To improve our understanding of the damage mechanism, dynamics of SWL-induced bubbles in constrained media were investigated. Silicone tubing and cellulose hollow fibers (i.d.=0.2 ~ 1.5 mm) were used to fabricate vessel phantoms, in which test fluid containing cavitation nuclei were circulated. Intraluminal bubble dynamics were examined by high-speed imaging and passive cavitation detection (PCD). Compared to the large expansion and violent inertial collapse of SWL-induced bubbles in a free field, the expansion of bubbles inside the vessel phantom is greatly constrained, leading to asymmetric elongation along the vessel axis and much weakened collapse. Conversely, the rapid, large expansion of the bubbles significantly dilates the vessel wall, leading to consistent rupture of the hollow fibers after less than 20 shocks in a XL-1 lithotripter. The rupture is dose-dependent, and varies with the spatial location of the vessel phantom inside the lithotripter field. Further, when the large intraluminal bubble expansion was suppressed by inverted lithotripter shock waves (LSW), the rupture could be avoided even after 100 shocks. Theoretical calculation confirms that the propensity of vascular injury due to LSW-induced intraluminal bubble expansion increases with the tensile pressure of the shock wave, and with the reduction of the inner diameter of the vessel, as noted in previous animal studies.

1. Introduction

Although SWL has been used routinely for the treatment of urolithiasis since 1980s, it also causes acute renal injury, which are primarily vascular lesions characterized by extensive damage of the endothelial cells and rupture of small blood vessels (Delius, 1994). To reduce the adverse effects of SWL, it is essential to understand the mechanisms of tissue injury, so that appropriate counteractive strategies may be developed. Currently, two different mechanisms have been implicated for tissue injury in SWL: cavitation and shear stress. For example, the cavitation mechanism is supported the spatial correlation between hyperechogenicity in B-scan ultrasound imaging (scattered from LSW-induced bubbles) and intrarenal hemorrhage (Kuwahara et al. 1989). Alternatively, shear stresses generated by wave scattering at a shock front propagating in heterogeneous medium has also been postulated to cause tissue injury (Howard and Sturtevant, 1997). Animal studies using inverted LSWs, which can significantly suppress bubble expansion, revealed minimal tissue damage after a clinical dose of shock wave exposure (Evan et al. 1998). This finding favors cavitation over shear stress as the primary mechanism for tissue injury in SWL.

The dynamics of LSW-induced cavitation in free field is characterized by an initial large and prolonged expansion, followed by subsequent violent collapse of the bubbles (Church 1989, Coleman et al. 1992). However, because of the limited space in tissue, the expansion of LSW-induced cavitation bubbles *in vivo* is significantly constrained (Zhong et al. 1998). Based on theoretical calculations, we have postulated that LSW-induced intraluminal bubble expansion could cause substantial dilation and may lead to rupture of small blood vessels, provided that appropriate cavitation nuclei exist in blood. To ascertain the mechanism of cavitation-induced vascular injury in SWL, it is essential to understand the dynamics of bubble oscillation in blood vessels.

In this work, we first investigated the dynamics of bubble oscillation inside vessel phantoms made of silicone tubing and cellulose hollow fibers of various sizes, in which test fluid containing cavitation nuclei were circulated. The phantom was immersed in an optically and acoustically transparent chamber filled with castor oil so that the intraluminal bubble activity could be visualized by high-speed imaging while the associated acoustic emission recorded by PCD. It was found that SWL-induced intraluminal bubble expansion is significantly constrained by the vessel wall, and consequently, the dilation of the vessel wall by the intraluminal bubble expansion leads to consistent rupture of the hollow fibers (i.d.= 0.2 mm) after less than 20 shocks. The rupture is dose-dependent, and varies with the spatial location of the vessel phantom in the lithotripter field. Further, when the large intraluminal bubble expansion was suppressed by inversion of the LSW, rupture of the hollow fiber could be avoided even after 100 shocks. These results support the hypothesis that rapid, large intraluminal bubble expansion may cause rupture of small blood vessels in SWL. In the second part, we evaluated the potential and the size-dependency of vascular injury due to intraluminal bubble expansion based on theoretical calculations of LSW-induced bubble dynamics in blood.

2. Experimental Design and Methods

2.1 Vessel phantoms

Silicone tubing (i.d.=0.3, 0.5, 1.0 and 1.5 mm, VWR, GA) and regenerated cellulose (RC) hollow fibers (i.d.=0.2 mm, Spectrum, CA) were used to construct vessel phantoms. The length of the phantom exposed in the acoustic field is about 34 mm, sufficiently wider than the 5-mm beam diameter of the XL-1 lithotripter. Each vessel phantom was connected to a circulation system running at a flowing rate of ~7.0 mm^3/s. To allow a clear observation of SWL-induced bubble dynamics inside the tube, degassed water (O_2<4 mg/L) containing 0.2% Albunex serving as cavitation nuclei was used as the test fluid. Further, the assembly was immersed in a 100-mm cubic test chamber (with a 115 μm thick polyester membrane bottom) filled with fresh castor oil to suppress cavitation outside the tube. The test chamber was placed on top of the XL-1 reflector, and the chamber has optical and acoustic windows on its lateral walls to facilitate high-speed imaging and PCD. The tube assembly was fixed on a three-axis translation stage for positioning (Fig. 1a). The tensile failure strength of the hollow fiber is σ_f=1.35 MPa, similar to that of the human thoracic aorta (σ_f=1.47~5.07 MPa) while σ_f for the silicone tubing is much higher (8.4 MPa).
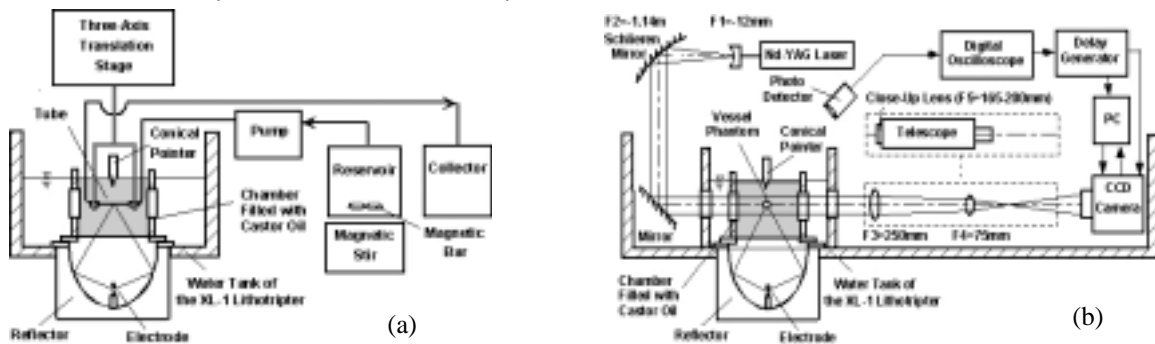

Fig.1 Schematic diagram of (a) the vessel phantom placed inside a test chamber filled with castor oil in the acoustic field of a XL-1 lithotripter and (b) experimental set up for high-speed imaging of bubble dynamics inside the vessel phantom.

2.2 High-speed imaging

Bubble dynamics was investigated using a high-speed imaging system shown in Fig. 1b. Both a low-magnification (for experiments in free field) and a high-magnification (for experiments in vessel phantoms) imaging system were established. A pulsed Nd:YAG laser (MiniLase-I, New Wave Research, CA) was expanded by a concave lens and collimated using a schlieren mirror to form a parallel light beam through the chamber. In each experiment, the spark discharge from the lithotripter electrode was picked up by a photodetector (PDA50, Thorlabs, NJ) and fed into a digital oscilloscope (9314, LeCroy, NY), which established a reference time for the whole event. The synchronized output of the oscilloscope was relayed to a digital delay generator (DS535, Stanford Research Systems, CA) to control the trigger of the pulsed laser, a CCD camera (GP-MF 552, Panasonic, NJ) and a frame grabber (DT3155, Data Translation, MA), respectively. By adjusting the delay time of the trigger signals, various stages of the bubble oscillation can be recorded.

2.3 Passive cavitation detection

Acoustic emission (AE) associated with SWL-induced bubble oscillation in free field and inside the vessel phantom was detected by PCD using 1 and 20 MHz focused transducers (Panametrics, MA), respectively. Their –6 dB reception zone (beam diameter x focal length) are 4.1×71 mm and 0.33×9.7 mm, respectively. The transducers were aligned orthogonal to the lithotripter and the vessel axes, and confocally with F_2. It was found that the small beam size of the 20 MHz transducer is essential for detecting AE emanating from inside the vessel phantoms, while avoiding picking up background noise in the test chamber during the shock wave exposure.

2.4 Rupture tests

The hollow fiber vessel phantom was immersed in the test chamber filled with freshly poured castor oil and exposed to LSWs at a low pulse repetition rate (< 0.1Hz). Before the release of each pulse, any visible bubbles outside the hollow fiber were removed. During the experiment, high-speed imaging was used to monitor the presence of intraluminal bubbles. The number of shocks needed to cause a rupture of the vessel phantom as well as the orientation of the rupture site were documented. If no rupture was produced after 100 shocks, the experiment was also terminated. At least six samples were used for each test configuration.

3. Experimental Results

3.1   Bubble dynamics

The general features of LSW-induced cavitation in a free field, as shown in Fig. 2a, are the initial rapid growth of cavitation bubbles in the wake of the incident shock front, bubble coalescence near their maximum expansion, and the subsequent violent collapse followed by a few rebounds. During the initial growth period, individual bubbles were almost spherical in geometry. Significant bubble aggregation occurs near the lithotripter axis, which leads to substantially increased maximum size and collapse time of the bubble cluster. The inertial collapse of the bubbles in a free field is violent, generating strong secondary shock wave emission (t=693μs in Fig. 2a). When a LSW was inverted, as shown in Fig. 2b, although bubbles were induced by the leading tensile wave, their expansion was quickly suppressed by the ensuing compressive wave, resulted in a substantially decreased maximum bubble size (~0.75 mm) and collapse time (~120 μs). Because of the significantly suppressed bubble activity, the inverted LSWs can be used to differentiate the contribution of cavitation from other potential mechanisms of tissue injury in SWL (Bailey et al. 1999).

In contrast to the large expansion in a free field, the expansion of LSW-induced bubbles in blood vessels will be constrained. As shown in Fig. 2c, the expansion of intraluminal bubbles inside a hollow fiber established contact with the fiber wall in less than 6 μs after the passage of the shock front. Subsequently, the rapid expansion of the bubbles was stopped in 2~3 μs, with presumably most of the remaining kinetic energy of the expanding bubble being absorbed by the fiber wall. After reaching the maximum expansion, the bubble collapsed in about 12 μs. Although the bubbles initially appeared in spherical geometry, they elongated substantially along the fiber axis during the constrained expansion. Because of the reduced maximum size and asymmetric deformation, the collapse of the bubbles inside the hollow fiber was greatly diminished compared to that in a free field (Fig. 2a). As expected, an inverted LSW greatly reduced the intraluminal bubble expansion and minimize the dilation of the fiber wall, with an apparent expansion-to-collapse period of the bubbles inside the fiber to be about 10μs (Fig. 2d).
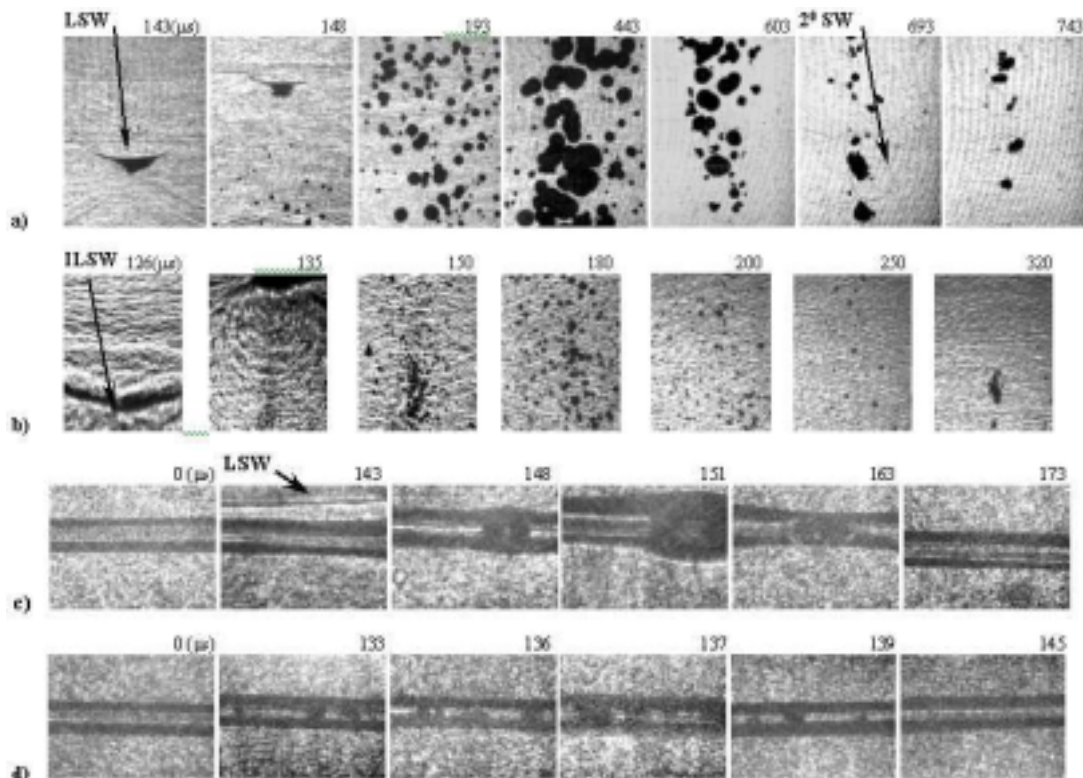

Fig. 2 Representative sequences of high-speed shadowgraphs of bubble dynamics produced at 24 kV (a) in free field produced by the standard lithotripter shock wave (LSW), (b) by the inverted LSW (ILSW), (c) in a 200-μm hollow fiber with LSW and (d) with ILSW. The number above each image frame indicates the time delay in μs after the spark discharge. The width of each frame in (a) is 15 mm.

3.2 Acoustic emission

Acoustic emission (AE) produced by the oscillation of cavitation bubbles in a lithotripter field has a characteristic double burst structure. The first burst corresponds to the initial compression and ensuing expansion of cavitation nuclei by the incident LSW while the second one corresponds to the subsequent inertial collapse of the bubbles. The collapse time of the bubble cluster (t_c) is defined by the time delay between the peak pressure of the two bursts. For the standard LSW at 24kV, the collapse time is about 525 μs and the peak pressure of the second AE burst is generally stronger than the first one. When the LSW was inverted, t_c was found to be significantly shortened (140 μs) and the second burst became much weaker. Fig. 3a shows the typical AE signals produced in water and inside hollow fiber using various reflector configurations. Moreover, the collapse time of LSW-induced bubbles inside the hollow fiber was found to be further reduced (~25 μs), independent of the lithotripter output voltage (Fig. 3b, 3c). Inversion of the LSW further shortens the t_c for the bubbles induced inside the hollow fiber (~12 μs). Overall, the temporal characteristics of the AE signals are in good agreement with the bubble dynamics in free water and inside the hollow fiber (Fig. 2). When castor oil was circulated inside the hollow fiber, the characteristic AE could not be detected and no intraluminal bubbles could be observed by high-speed imaging during SWL.

Fig. 3c summarizes the measured t_c for LSW-induced bubbles both in free field and constrained media. In water, the value of t_c (mean±s.d.) was observed to increase with the lithotripter output voltage, from 386±24 μs at 16 kV to 583±23 μs at 24 kV. In the vessel phantoms, although t_c was reduced in general, the degree of reduction depends critically on the size of the vessel phantom. In large silicone tubing (i.d.>1.0 mm), despite of the constraint, the value of t_c still increased monotonically with the lithotripter output voltage. Yet, in small vessel phantoms (i.d.<0.3 mm), the constraining effects on intraluminal bubble expansion became much more pronounced. Inside the hollow fiber, the bubble collapse time was found to be statistically independent of the lithotripter output voltage ($p<0.05$). All together, these results demonstrate that the vessel constraint on intraluminal bubble expansion is size-dependent, and the constraint increases dramatically when the inner diameter of the vessel becomes less than 300 μm.
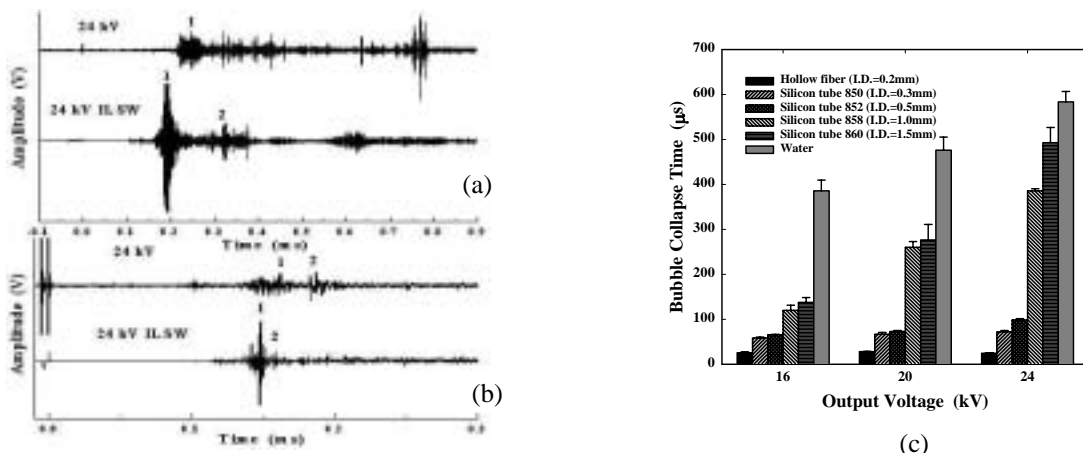

Fig. 3 Typical acoustic emission signals produced (a) in free field, (b) in hollow fibers, using either standard or inverted LSW at 24kV, (c) comparison of bubble collapse time (t_c) in water, silicone tubings, and hollow fibers at various output voltages of the XL-1 lithotripter.

3.3 Rupture of hollow fibers

Using the standard reflector, rupture of the hollow fibers placed at F_2 was observed consistently within 20 shocks at various output voltage settings (Fig. 4a), and no strong directional preference in the orientation was detected (Fig. 4b). Optical microscopy revealed that the rupture is mainly in the form of a cleft along the axial direction of the hollow fiber (Fig. 5), which is typical for failure due to circumferential stretching such as that produced by internal pressurization. The cleft increases significantly from ~100 to 600 μm as the output voltage of the lithotripter increases from 16 to 24 kV. On the other hand, when the large dilation of the fiber wall was suppressed by inverted LSW or by filling the hollow fiber with castor oil, no rupture could be produced even after 100 shocks. All these results support the hypothesis that the rupture is caused by the large intraluminal expansion of cavitation bubbles. In contrast, if the damage were caused by the collapse of bubbles impinged by the LSW, predominance of the rupture along the lithotripter axis and a much smaller rupture site would be expected.

In addition, the rupture of the hollow fiber was found to vary with its spatial location in the lithotripter field, along the shock wave axis from z=-10 mm to z=2.5 mm (Fig. 6). However, the propensity of the rupture was found to be

higher prefocally than postfocally. This is likely caused by the nonlinear propagation of LSWs which shifts the negative peak pressure towards the lithotripter generator (Averkious and Cleveland, 1999).

Using high-speed images recorded during the rupture experiments, the maximum circumferential strain (ε_M) imposed on the fiber wall by the intraluminal bubble expansion was determined. Assuming that the fiber wall was elastically deformed before the rupture, the circumferential stress would be proportional to ε_M. The results in Fig. 7 revealed that ε_M increases with the output voltage of the lithotripter. However, the maximum axial stain is much smaller than the corresponding circumferential strain. These results are consistent with the damage pattern of the hollow fiber (Fig. 5), which could be generated by the predominant circumferential stretching of the fiber wall due to intraluminal bubble expansion. The general trend in ε_M vs. N_r (the number of shocks needed to cause a rupture) curve is typical for material failure under cyclic loading. For the inverted LSW, the dilation is so small that a much higher number of shocks would be required to cause a rupture, as indicated by our experimental observation. Overall, we conclude that the rupture of the hollow fiber depends on the shock wave dosage, spatial location, and pressure waveform of the lithotripter field, and the rupture is most likely caused by the intraluminal expansion of cavitation bubbles.
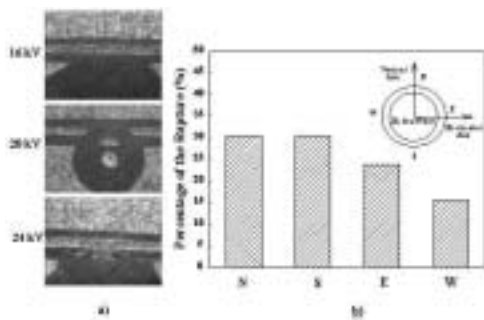

Fig. 4 Rupture of hollow fibers after shock wave exposure, (a) leakage of circulating fluid, and (b) orientation of rupture in the vessel phantom.
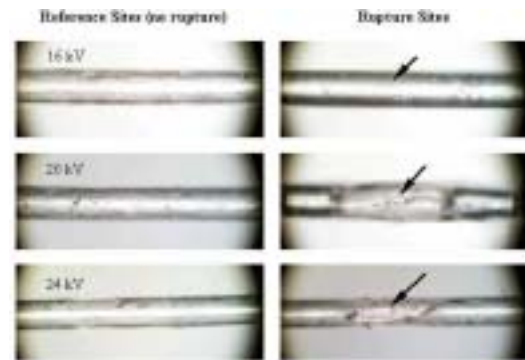

Fig. 5 Optical micrographs of the hollow fibers after shock wave exposure. The damage pattern is characterized by a cleft along the axial direction of the fiber.
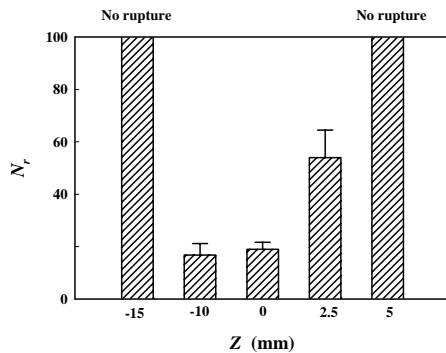

Fig. 6 Spatial-dependence of the rupture of the hollow fibers. The number of shocks needed to cause a rupture (N_r) is significantly higher prefocally than postfacally. Outside the beam focus (z<-15mm or Z>5mm) no rupture could be produced even after 100 shocks.
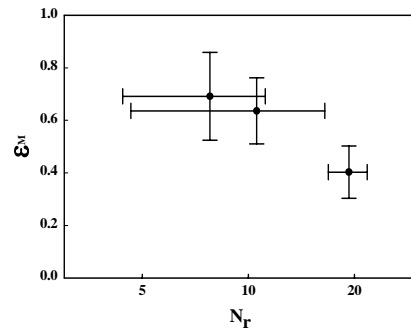

Fig. 7 Relationship between the maximum circumferential strain ε_M imposed on the fiber wall by the intraluminal bubble expansion and the number of shocks needed to cause a rupture (N_r).

4. Theoretical Assessment of Bubble Dynamics in Blood

If appropriate cavitation nuclei (initial radius $R_0 > 10$ nm) exist in blood, theoretical calculations have shown that inertial cavitation can be induced in the blood vessels near the beam focus of a clinical HM-3 lithotripter (Zhong et al. 1998). Without tissue constraint, the shock wave-excited bubbles in blood could reach a maximum diameter between 1.3 mm and 2.3 mm, depending on the tensile pressure of the LSW. Since this potential bubble expansion greatly exceeds the size of typical small blood vessels in the kidney, it has been postulated that significant dilation of the vessel wall would occur, which may lead to the rupture of the vessel (Zhong et al. 1998). This hypothesis is

confirmed in this study using the hollow fiber vessel phantom. To gain further theoretical insights on the damage mechanism, it is important to understand the mechanical interaction between an intraluminal bubble and the surrounding tissue structure. A model for such an interaction, however, has not been developed because of the complex mathematical treatment needed to describe the dynamics of asymmetric bubble oscillation inside an elastic or viscoelastic tubular structure. We, therefore, assume that it is reasonable to use a spherical bubble model to simulate the bubble expansion up to the point of contact and to assess qualitatively the potential of the ensuing bubble-vessel interaction on vascular injury based on the remaining energy of the expanding bubble. The clinically relevant goal of such an investigation is to assess the effect of vessel size on SWL-induced injury.

The Gilmore model was used to simulate the radial oscillation of a LSW-induced spherical bubble in blood (assuming without tissue constraint):

$$R(1-\frac{U}{C})\frac{dU}{dt}+\frac{3}{2}(1-\frac{U}{3C})U^2=(1+\frac{U}{C})H+\frac{1}{C}(1-\frac{U}{C})R\frac{dH}{dt} \tag{1}$$

where R is the bubble radius, U is the velocity of the bubble wall, C and H are the sound speed in the liquid at the bubble wall and the enthalpy difference between the liquid at pressure at the bubble wall $P(R)$ and the pressure at infinity P_∞, respectively. The relation between $P(R)$ and the gas pressure inside the bubble (P_g), liquid viscosity (μ), and surface tension (σ) in the liquid is given by $P(R)=(P_0+\frac{2\sigma}{R_0})(\frac{R_0}{R})^{3\eta}-\frac{2\sigma}{R}-\frac{4\mu}{R}U$, and $P_\infty=P_0+P_S$ where P_0 is the

ambient pressure of the surrounding liquid, R_0 is the initial equilibrium radius of the bubble, η is the polytropic exponent of the gas, and P_S is a LSW produced in the liquid far away from the bubble. Because we are interested in the expansion phase of the bubble dynamics, gas diffusion across the bubble wall, which has been shown to only affect significantly the collapse of the bubble (Church, 1989), is not considered.

The Gilmore model (Eq. 1) was nondimensionalized and solved using the 5th-order Runge-Kutta-Fehlberg method with a step-size control algorithm (Zhu and Zhong, 1999). For the numerical calculation, the following parameters of the blood were used: $\rho_0=1059$kg/m^3, $\mu=5\times10^{-3}$ kg/m·s, $\sigma=56\times10^{-3}$N/m, and $C_0=1584$ m/s. Once the bubble dynamics in a free field were determined, the work done by the bubble during the expansion phase from the bubble radius at contact (R_c) to the maximum radius (R_{max}) against ambient pressure (E_{p0}), surface tension (E_σ), and viscous force (E_μ) were calculated using the following equations:

$$E_{p_0}=\int_{R_c}^{R_{max}}P_0 4\pi R^2 dR=\frac{4}{3}\pi(R_{max}^3-R_c^3)p_0 \tag{2}$$

$$E_\sigma=\int_{R_c}^{R_{max}}\left(\frac{2\sigma}{R}\right)4\pi R^2 dR=4\pi(R_{max}^2-R_c^2)\sigma \tag{3}$$

$$E_\mu=\int_{R_c}^{R_{max}}\left(\frac{4\mu}{R}U\right)4\pi R^2 dR \tag{4}$$

The kinetic energy of the mass of fluid surrounding the expanding bubble can be calculated by,

$$E_k=\frac{1}{2}M_{eff}U^2 \tag{5}$$

where $M_{eff}=3\rho_0(4\pi/3)R^3$ is the effective mass "felt" by the bubble, when the acoustic wavelength is larger than R. Since the gas pressure inside the bubble ($P_g\propto(R_0/R)^{3\eta}$) drops quickly during bubble expansion and becomes much smaller than P_0, the internal energy of the gas in the bubble expansion is negligible compared to E_{p_0}.

Fig. 8 shows the typical response of a 3-μm cavitation nucleus in blood (assuming without tissue constraint) to different pressure waveforms in a HM-3 lithotripter field. To account for tissue attenuation, the peak positive pressure (P^+) was reduced by 25% from typical values in water. While the peak negative pressure (P^-) was varied from -4 MPa to -10 MPa, similar to the values measured in water since the effect of tissue attenuation on the tensile pressure is small. The computed bubble dynamics is characterized by an initial rapid, large expansion of the bubble following the tensile pressure of the incident LSW, with the bubble size increasing by about two orders of magnitude within the first 10 μs. This feature is in accordance with the experimental observation of the LSW-induced bubble expansion in the hollow fiber (Fig. 2c). In general, both the maximum radius and collapse time of the bubble in blood were found to increase, as the tensile pressure of the LSW becomes stronger. These results suggest that the propensity of vessel rupture due to intraluminal bubble expansion will be higher in regions of the kidney where the peak tensile pressure of the LSW is produced.

The bubble wall velocity U vs. R, is shown in Fig. 9 for the initial expansion and a portion of the subsequent collapse of the bubble, with the response of the cavitation nucleus to the leading compressive pressure ($P^+=30$ MPa, $t^+=1$ μs) of the LSW shown in the insert. It consists of a rapid implosion, an immediate rebound, followed by a

series of oscillations before both *U* and *R* increase monotonically. Subsequently, the tensile pressure ($P^- =$-10 MPa, $t^- =$5 μs) of the LSW causes the bubble to expand significantly, in a time scale much longer than the pulse duration of the LSW. However, the bubble wall only accelerates outwards in the initial short period, but decelerates in the remaining prolonged period of the bubble expansion. The maximum expanding velocity of the bubble wall was calculated to be 50, 66 and 81 m/s, as the magnitude of P^- increases from -4, -7 to -10 MPa, respectively. The corresponding bubble radii for the maximum *U* were 44, 100 and 130 μm, which are quite small compared to the corresponding bubble radii (398, 766 and 1,141 μm,) at the maximum expansion.
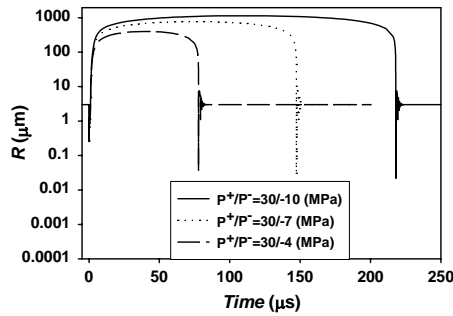

Fig. 8   Computed responses of a cavitation nucleus (R_0=3μm) to various pressure waveforms in the acoustic field of a HM-3 lithotripter. The peak positive pressure was derated from typical values measured in water to account for tissue attenuation.
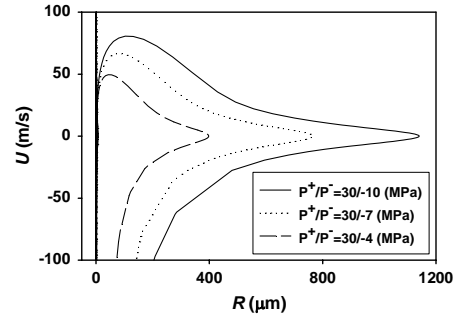

Fi   adius (*R*), in response to various acoustic field of a HM-3 lithotripter. The inserted figure shows the initial response of the bubble nucleus to the compressive pressure of the incident shock wave.
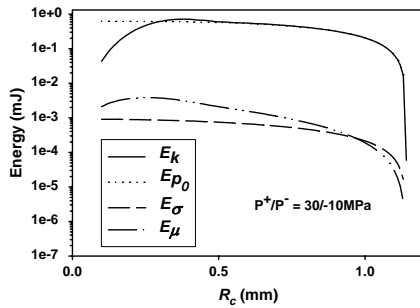

Fig. 10   The work done by an expanding bubble against ambient pressure (E_{p0}), surface tension (E_σ), and viscous force (E_μ), as well as the kinetic energy of the fluid surrounding the bubble (E_k) in relation to the bubble radius at contact (R_c).
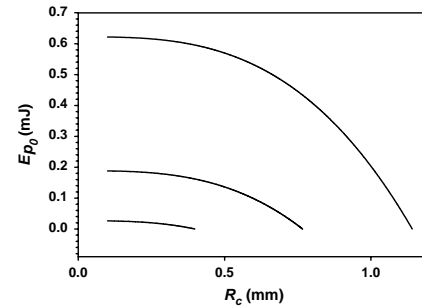

Fig. 11   Relationship between the potential energy of the bubble (E_{p0}) and the bubble radius at contact (R_c).

During expansion, the work done by the bubble against ambient pressure (E_{p0}), surface tension (E_σ) and viscous force (E_μ) drop monotonically with R_c, although initially E_μ may increase slightly if R_c is smaller than 300 μm (Fig. 10). Similarly, the kinetic energy of the fluid surrounding the bubble, E_k, will increase initially reaching a maximum at R_c = 400 μm and then decrease monotonically with R_c. In comparison, E_{p0} and E_k are at least two orders of magnitude greater than E_σ and E_μ, so that most of the energy provided by the LSW are converted into the kinetic and potential energy ($E_k + E_{p0}$) of the expanding bubble. The close match between E_k and E_{p0} when R_c is greater than 500 μm indicates that in the later stage of the expansion, the kinetic energy of the bubble was converted into the potential energy. Qualitatively, if a cavitation bubble were produced in a blood vessel, the energy carried by the expanding bubble at the moment of contact would be higher in a small vessel than in a large one. As the vessel size increases, the energy associated with the potential bubble expansion will be reduced in proportion to R_c^3 (Eq. 5 and Fig. 11). Furthermore, when the tensile pressure of the LSW is reduced, the energy associated with the potential bubble expansion will drop significantly, indicating that the propensity of vessel rupture depends on both the output voltage of the lithotripter and the spatial location of the vessel in the lithotripter field. These predictions are verified by the experimental results shown in Figs. 6-7.

5. Discussion

Although cavitation is often considered as an important contributory factor for tissue injury in SWL (Delius 1994), the underlying mechanism has not been well understood. In this work, we developed vessel phantoms made of silicone tubing and RC hollow fibers immersed in castor oil so that LSW-induced intraluminal bubble activity and bubble-vessel interaction can be quantified by high-speed imaging and PCD techniques, and the resultant damage can be readily determined. Using this approach, we have demonstrated a size-dependent vessel constraining effect on LSW-induced bubble expansion, which leads to significantly reduced maximum expansion and collapse time of the bubbles compared to that produced in a free field. Furthermore, in small vessels (modeled by the hollow fibers), the large expansion of the intraluminal bubbles was found to cause significant dilation and consistent rupture of the vessel wall within 20 shock wave exposure. As either the pressure amplitude of LSW increases or the vessel size becomes smaller, the propensity for vessel rupture due to intraluminal bubble expansion will increase substantially. In contrast, when the large expansion of the intraluminal bubbles was suppressed by inverted LSW, the dilation of the hollow fiber was significantly reduced, and no rupture could be produced even after 100 shocks. All these results confirm the hypothesis that the rupture of small blood vessels in SWL is caused primarily by the rapid, large expansion of intraluminal bubbles. This mechanism of vascular injury is distinctly different from the classic theory of cavitation damage in unconstrained media where damage is often attributed to the strong shock wave emission or microjet impact due to the violent collapse of inertial bubbles.

Although the size and distribution of cavitation nuclei in the vasculature is currently unknown, inertial cavitation induced by LSWs in the intrahepatic branches of the portal vein and tributaries of hepatic veins has been observed (Delius et al. 1990). Once a bubble is induced, it may generate multiple smaller bubbles upon collapse (Church, 1989), and therefore, provides more cavitation nuclei in the blood for the ensuing LSWs if the interpulse delay is not too long. As our experimental data and theoretical calculations have suggested that if adequate cavitation nuclei exist in the blood, the propensity of vessel rupture is particularly high for capillaries and small blood vessels. In large blood vessels, when the residual bubbles becomes larger than 0.5 mm in diameter, shock wave-bubble interaction with resultant high-speed microjet impingement may also lead to the perforation of the vessel (Philipp et al. 1993).

One method that has been shown to minimize tissue injury is the inversion of LSW (Evan et al. 1998). Unfortunately, the inverted LSW does not produce stone comminution. Based on theoretical calculation, it appears that a feasible approach to reduce tissue injury while maintaining adequate fragmentation capability of the LSWs is the selective reduction of the tensile pressure of the LSW (Zhu and Zhong, 1999).

In summary, using vessel phantoms made of silicone tubing and RC hollow fibers we have demonstrated a size-dependent vessel constraining effect on LSW-induced bubble expansion. Conversely, the rapid, large expansion of intraluminal bubbles was found to cause substantial dilation of the vessel wall, leading to consistent rupture of the vessel after a low dose of shock wave exposure. Finally, suppression of the large bubble expansion prevents vessel rupture, indicating potential remedy to minimize tissue injury in SWL.

Acknowledgements

References

Averkiou MA and Cleveland RO. (1999) *J. Acoust. Soc. Am.*; **106,** 102-112.
Bailey MR, Blackstock DT, Cleveland RO, and Crum LA. (1999). *J. Acoust. Soc. Am.*, **106**, 1149-1160.
Church CC. (1989). *J. Acoust. Soc. Am.*, **86**, 215-227.
Coleman AJ, Choi MJ, Saunders JE, and Leighton TG. (1992). *Ultrasound Med. Biol.,* **18**, 267-281.
Delius M et al. (1990), *Ultrasound Med. Biol.,* **16**, 467-472.
Delius M. (1994). *Shock Waves*, **4**. 55-72.
Evan A et al. (1998), *J. Acoust. Soc. Am.,* **103**, 3037.
Howard D. and Sturtevant B. (1997) *Ultrasound Med. Biol.,* **23**, 1107-1122.
Kuwahara M, et al. (1989). *J. Lithotripsy Stone Dis.,* **1**, 218-288.
Philipp A, Delius M, Scheffczyk C, Vogel A, and Lauterborn W. (1993), *J. Acoust. Soc. Am.,* **93,** 2496-2509.
Zhong P, Cioanta I, Zhu SL, Cocks FH, and Preminger GM. (1998), *J. Acoust. Soc. Am.,* **104**, 3126-3129.
Zhu SL and Zhong P. (1999), *J. Acoust. Soc. Am.,* **106,** 3024-3033.